Journal of
Materials Chemistry A

PAPER

View Article Online
View Journal | View Issue

Cite this: *J. Mater. Chem. A*, 2016, **4**, 3907

Terbium doped ZnCr-layered double hydroxides with largely enhanced visible light photocatalytic performance†

Yi Fu, Fanyu Ning, Simin Xu, Hongli An, Mingfei Shao* and Min Wei

Received 10th December 2015
Accepted 6th February 2016

DOI: 10.1039/c5ta10093c

www.rsc.org/MaterialsA

Recently, layered double hydroxides (LDHs) have emerged as highly active photocatalysts due to their unique structure, large specific surface area and semiconductor properties. However, the slow interfacial kinetics and fast charge recombination are the major obstacles which limit the performance of LDH-based photocatalysts. Here, we demonstrate the doping of rare earth ions into the host layer of LDHs to inhibit the charge recombination and increase the charge injection efficiency simultaneously. A series of terbium ion (Tb^{3+}) doped ZnCr–LDHs (Tb-ZnCr–LDHs) have been successfully synthesized *via* a co-precipitation method, and their photocatalytic water splitting activities were evaluated under visible light irradiation. The sample with a Tb^{3+} doping content of 0.5% (molar ratio) shows optimal performance for oxygen evolution (1022 μmol h^{-1} g^{-1}) among all these Tb-ZnCr–LDH materials. The photoluminescence and photoelectrochemistry measurements over the Tb-ZnCr–LDH samples prove effective separation of photo-induced charge carriers and high charge injection efficiency, compared with a pristine ZnCr–LDH. This strategy can be applied to modify other photocatalysts toward low-cost solar fuel generation systems.

Introduction

Photocatalytic water splitting for the generation of hydrogen and oxygen has attracted considerable attention for clean and renewable energy production without fossil fuel consumption and carbon dioxide emission.[1] In the past decades, numerous photocatalysts have been explored for water splitting utilizing solar energy, such as metal oxides,[2] nitrides[3] and sulfides.[4] Although these materials have shown interesting performance, the efficiency of the photocatalytic process generally suffers from limited light absorption, poor charge transport properties or sluggish interfacial kinetics toward water splitting.[5] Recently, considerable efforts have been focused on this issue by metal[6] or non-metal[7] ion doping, modification with semiconductors[8,9] or loading of water splitting cocatalysts (*e.g.* Co_3O_4 (ref. 10) and Co-Pi (ref. 11)). Nevertheless, achieving cost-effective photocatalysts with high performance and desirable stability for water splitting remains a challenging goal.

Layered double hydroxides (LDHs) are typical two-dimensional (2D) inorganic materials generally expressed by the formula $[M^{II}_{1-x}M^{III}_{x}(OH)_2]^{x+}(A^{n-})_{x/n}\cdot mH_2O$ (M^{II} and M^{III} refer to bivalent and trivalent metal cations; A^{n-} refers to interlayer exchangeable anions).[12] Recently, LDHs have been investigated as photocatalysts (*e.g.* ZnTi–LDHs,[13] NiTi–LDHs[14,15] and ZnCr–LDHs[16]), owing to their unique intercalation structure with highly dispersed metal cations, large specific surface area and remarkable adsorption capacity. So far, several important strategies have been developed for improving LDH-based photocatalysts by tuning the composition of host layers,[17] intercalating guest sensitizers,[18] and constructing hierarchical nanocomposites.[19] However, serious recombination of photo-induced charge carriers is inevitable for most LDH-based photocatalysts due to the poor charge mobility of traditional LDHs. Therefore, efforts for facilitating photo-induced electron–hole separation and improving the interfacial kinetics of LDH-based photocatalysts are highly necessary.

Lanthanides are renowned for their abundant 4f electrons and strong coordination abilities.[20] When integrated into a semiconductor matrix, they can serve as adsorption sites for reactants or create lattice distortion to enhance the separation of photo-induced electron–hole pairs.[21] If appropriate lanthanide metal ions are doped into the host layer of LDHs,[22–24] the photocatalytic performance of LDHs would be ameliorated as a result of the enhanced charge separation efficiency. In addition, the vacant d-orbitals of rare earth elements and the distortion of the lattice may contribute to the surface charge injection process,[25] which is of great importance for the photocatalytic reaction. In spite of a large potential, the lanthanide-doped LDH materials and their photocatalytic properties have seldom been studied so far.

State Key Laboratory of Chemical Resource Engineering, Beijing University of Chemical Technology, Beijing 100029, P. R. China. E-mail: shaomf@mail.buct.edu.cn; Fax: +86-10-64425385; Tel: +86-10-64412131

† Electronic supplementary information (ESI) available: FT-IR spectra, ICP-AES, N_2 sorption analysis, SEM and TEM images, and results of photoelectrochemical measurements are included. See DOI: 10.1039/c5ta10093c

Herein, a series of Tb^{3+} doped ZnCr–LDHs (denoted as Tb-ZnCr–LDHs) have been synthesized *via* a facile co-precipitation method, which exhibit largely enhanced photocatalytic water oxidation performances under visible light. The as-synthesized Tb-ZnCr–LDH possesses a 2D plate-like morphology with a lateral particle size of ~50 nm and a thickness of ~2 nm. It is found that the sample with a Tb doping ratio of 0.5% displays superior photocatalytic activity for the water oxidation under visible-light irradiation, with a much higher photo-induced charge separation efficiency and stronger photocurrent response compared with pristine ZnCr–LDH, as confirmed by photoluminescence and photoelectrochemical measurements. Thus, this work provides a promising route for the enhancement of photo-response ability and charge injection efficiency of LDH-based photocatalysts under visible light irradiation by introducing rare earth ions.

Experimental section

Materials

Analytical grade chemical reagents including $Zn(NO_3)_2\cdot6H_2O$ (AR, 99%), $Cr(NO_3)_3\cdot6H_2O$ (AR, 99%), $Tb(NO_3)_3\cdot5H_2O$ (metal basis, 99.99%), $AgNO_3$ (AR, 99.8%) and H_2O_2 (AR, 30 wt%) were purchased from Aladdin reagent Co. Ltd. NaOH (AR, 99.5%), Na_2CO_3 (AR, 99.5%), and Na_2SO_4 (AR, 99.5%) were obtained from Beijing Chemical Co., Ltd. Deionized water was used in all the experimental processes.

Synthesis of Tb-ZnCr–LDHs

The Tb-ZnCr–LDHs with various molar ratios (r) of $Tb^{3+}/(Tb^{3+} + Cr^{3+})$ ($r = 0\%$, 0.1%, 0.5%, 1%, and 5%) were prepared by a co-precipitation method, which were denoted as LDH-0%, LDH-0.1%, LDH-0.5%, LDH-1%, and LDH-5%, respectively. Typically, aqueous solution A containing $Zn(NO_3)_2\cdot6H_2O$ (0.2 M), $Cr(NO_3)_3\cdot6H_2O$ and $Tb(NO_3)_3\cdot5H_2O$ ($N_{Tb} + N_{Cr} = 0.1$ M) and aqueous solution B containing 1 M NaOH and 0.5 M Na_2CO_3 were first prepared. Then solutions A (50 mL) and B (30 mL) were simultaneously added into 100 mL of deionized water, and the pH of the suspension was maintained at approximately 9. The resulting slurry was transferred into a Teflon-lined stainless steel autoclave and hydrothermally treated at 120 °C for 24 h. The final precipitate was filtered, washed thoroughly with deionized water and dried at 60 °C for 24 h. The product yields for the synthesized LDH-0%, LDH-0.1%, LDH-0.5%, LDH-1%, and LDH-5% are 97.8%, 97.5%, 97.5%, 97.3%, and 97.1%, respectively.

Photocatalytic tests

The photocatalytic experiments were conducted in a 50 mL Pyrex flask. Typically, the photocatalyst (45 mg) was dispersed in aqueous solution (45 mL), with $AgNO_3$ (0.01 M) as a sacrificial reagent. An airtight silicon stopper was used to seal the headspace of the reactor, and the suspension was purged with argon for 30 min. Then the reaction was conducted under the illumination of a xenon arc lamp (150 W; Beijing AuLight Co., Ltd.) with a UV cutoff filter ($\lambda > 420$ nm). Water bath equipment kept at 40 °C was used to avoid the ambient temperature variation influence. The oxygen was identified by injecting the reactor headspace gas into a gas chromatograph (GC-7890II; Tech-comp. Co., Ltd.) operating under isothermal conditions (30 °C) equipped with a semicapillary column and a thermal conductivity detector.

Photoelectrochemical water splitting measurements

All photoelectrochemical (PEC) water splitting studies were carried out at an electrochemical workstation (CHI 660C, CH Instruments Inc., Shanghai) in a home-built three-electrode optical cell, by using Hg_2Cl_2 as the reference electrode, a Pt wire as the counter electrode and ITO coated LDH (area: 2 cm^2) as the working electrode. The working electrode was fabricated as follows: 1 mg of LDHs was dispersed in 1 mL ethanol solution; 200 μL of the suspension was dripped onto the ITO surface and dried for 15 min; 100 μL of 5% Nafion (Sigma–Aldrich) was coated onto the surface and dried for 10 min. Measurements were performed in a 0.5 M Na_2SO_4 (pH = 6.8) solution by cyclic voltammetry in the potential range from 0 V to +0.7 V. The Tb-ZnCr–LDH photoelectrodes were illuminated at 100 mW cm^{-2} using a 150 W xenon lamp with a UV cutoff filter ($\lambda > 420$ nm). Amperometric I–t curves of LDHs were recorded at an applied voltage of +0.6 V.

Characterization

Powder X-ray diffraction patterns of the synthesized samples were collected on a Shimadzu XRD-6000 diffractometer using a Cu Kα source, with a scan step of 0.02 degree and a scan range between 3 degrees and 70 degrees. Fourier transform infrared (FT-IR) spectra were collected using a Vector22 (Bruker) spectrophotometer with 2 cm^{-1} resolution in the range between 4000 and 400 cm^{-1}. X-ray photoelectron spectra (XPS) were recorded on a Thermo VG ESCALAB250 X-ray photoelectron spectrometer at a pressure of about 2×10^{-9} Pa using Al Kα X-rays as the excitation source. The morphology of the samples was investigated using a scanning electron microscope (SEM; Zeiss Supra 55) with an accelerating voltage of 20 kV, combined with an energy dispersive X-ray spectrometer (EDX) for the determination of metal composition. The specific surface area determination and pore volume and size analysis were performed by Brunauer–Emmett–Teller (BET) and Barrett–Joyner–Halenda (BJH) methods using a Quantachrome Autosorb-1C-VP Analyzer. Prior to the measurements, the samples were degassed at 100 °C for 8 h. Solid-state UV-vis diffuse reflectance spectra were recorded at room temperature in air by means of a Shimadzu UV-3000 spectrometer in the 200–800 nm wavelength range. The samples (100 mg) were pressed into pellets with a diameter of 1 cm and 0.1 cm in thickness under a pressure of 8 MPa. Fluorescence emission spectra were recorded using a fluorophotometer (RF-5301PC, 1.5 nm resolution) in the range of 380–570 nm with an excitation wavelength of 350 nm and slit widths of 3 nm. Transmission electron microscopy (TEM) images were recorded with Philips Tecnai 20 and JEOL JEM-2010 high-resolution transmission electron microscopes.

The electron spin resonance (ESR) data were recorded on a JES-FA200 Electron Spin Resonance Spectrometer, JEOL.

Results and discussion

The Tb-ZnCr–LDHs were prepared *via* a co-precipitation method, and the structure was confirmed by powder X-ray diffraction (XRD) measurements (Fig. 1). The Bragg reflections of the LDHs with various contents of Tb can be indexed to a hexagonal lattice with a $R3m$ rhombohedral symmetry with basal reflection planes (003), (006), (012), (110) and (113),[26] and no obvious impurity phase was found. The basal spacing of the LDHs (d_{003}) is ~0.75 nm, which is close to the value of carbonate-intercalated LDHs.[27,28] Fig. 1b shows high resolution patterns of (110) and (113) reflections of the Tb-ZnCr–LDH. Lattice parameters $a = 2d_{110}$ and $c = 3d_{003}$ were calculated and are summarized in Table 1. The value of parameter a ($a = 2d_{110}$), which refers to the distance of adjacent metal cations, increases gradually along with the progressive enhancement of the Tb^{3+} content from 0% to 1%. This implies the successful doping of Tb^{3+} into the brucite layer of the ZnCr–LDH. However, the parameter a remains unchanged when the doping content is larger than 1%, indicating that a limited amount of Tb can be introduced into the LDH host layer. Tb^{3+} has a much larger ionic radius of 92 pm than Cr^{3+} (62 pm). An isomorphic substitution of Cr^{3+} by Tb^{3+} would induce a lattice distortion that is unfavorable in energy; therefore only a limited doping of Tb^{3+} can be achieved.[29–31]

The obtained LDHs were further characterized by Fourier translation infrared (FT-IR) spectroscopy (Fig. S1†). A broad absorption band at ~3410 cm^{-1} is due to the stretching vibrations of surface hydroxyl groups and the interlayer water molecules. Bands at ~1360 cm^{-1} (ν_3) and ~860 cm^{-1} (ν_2) are assigned to the vibrations of carbonate.[32] The weak shoulder at ~1045 cm^{-1} can be ascribed to mode ν_1 of carbonate.[33] Other bands in the range of wavenumbers less than 1000 cm^{-1} (786, 575 and 515 cm^{-1}) are ascribed to the translational mode vibrations of metal–O and metal–O–metal.[34] In general, the FT-IR spectra show no obvious difference for the Tb doped ZnCr–LDH and pristine ZnCr–LDH, indicating that the structure and symmetry of LDHs are well maintained after Tb doping. This is consistent with the XRD results.

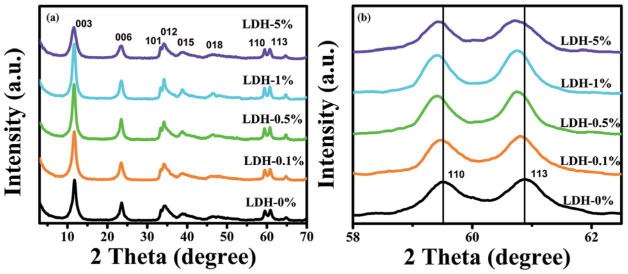

Fig. 1 (a) Powder XRD patterns of ZnCr–LDH samples with different doping molar ratios of Tb^{3+} (denoted as LDH-0%, LDH-0.1%, LDH-0.5%, LDH-1% and LDH-5%, respectively); (b) high resolution XRD patterns of (110) and (113) reflections of the as-synthesized samples.

Table 1 Cell parameters of various Tb-ZnCr–LDH samples

	Lattice parameter			
Catalyst	d_{003} (Å)	d_{110} (Å)	a (Å)	c (Å)
LDH-0%	7.5320	1.5532	3.1064	22.5960
LDH-0.1%	7.5345	1.5547	3.1094	22.6035
LDH-0.5%	7.5698	1.5562	3.1124	22.7094
LDH-1%	7.5825	1.5560	3.1120	22.7475
LDH-5%	7.6076	1.5559	3.1119	22.8228

X-ray photoelectron spectroscopy (XPS) was used to figure out the electronic properties of the prepared LDHs (Fig. 2). The electron transfer trend between the two elements can be deduced by the change of the chemical state obtained from XPS results.[35,36] The corresponding peaks of Cr 2p in the Tb-ZnCr–LDH exhibit an apparent shift of ~0.5 eV to lower binding energy (Fig. 2a), which can be ascribed to the enhanced electron density of Cr due to the introduction of Tb^{3+} into the ZnCr–LDH.[37] Similarly, a shift of 0.3 eV to lower binding energy is also observed for the O 1s (Fig. 2b). In contrast, no obvious shift occurs for the binding energy of Zn 2p, indicating the absence of electron transfer of Zn (Fig. 2c). Thus, the incorporation of Tb into the LDH host layer induces electron transfer from Tb to Cr, which would play an important role in the photocatalytic performance. In addition, the peak intensity of Tb 3d$_{5/2}$ and 3d$_{1/2}$ at 1244.0 eV and 1279.1 eV increases gradually along with the enhancement of doped Tb^{3+} (Fig. 2d), implying the involvement of Tb^{3+} into the lattice of the ZnCr–LDH. The results above indicate that the incorporation of Tb^{3+} into the ZnCr–LDH matrix leads to a decrease in the positive potential of Cr and O, which could provide a favourable environment for the transference of photo-induced electrons and holes.

SEM coupled with EDX and TEM images of the Tb-ZnCr–LDH are shown in Fig. 3. SEM images of the Tb-ZnCr–LDH show the presence of 2D nanoflakes with a lateral size of 30–50 nm

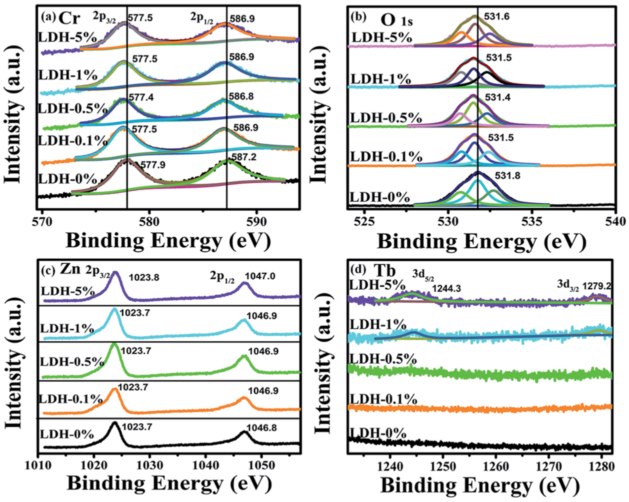

Fig. 2 XPS spectra of (a) Cr 2p, (b) O 1s, (c) Zn 2p and (d) Tb 3d for the various Tb-ZnCr–LDH samples.

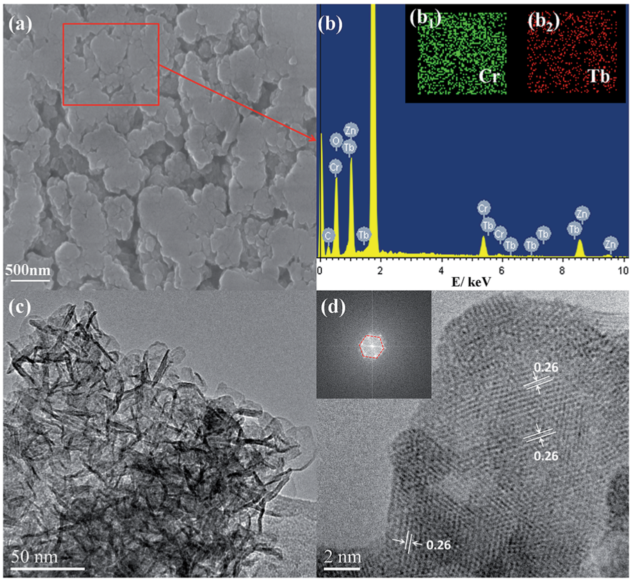

Fig. 3 (a) SEM image of the ZnCr–LDH with a Tb doping molar ratio of 0.5% (LDH-0.5%). (b) The corresponding EDX spectrum, and elemental mapping images of (b_1) Cr and (b_2) Tb. (c) TEM image and (d) HR-TEM image of LDH-0.5%, with the SAED pattern shown in the inset of panel (d).

(Fig. 3a and S2†), which is nearly the same as that of the pristine ZnCr–LDH. The EDX analysis of LDH-0.5% demonstrates the presence of Zn, Cr and Tb, and the elemental mapping images suggest that Cr and Tb are highly dispersed (Fig. $3b_1$ and b_2). The chemical compositions of these Tb-ZnCr–LDH samples are further studied by inductively coupled plasma-atomic emission spectroscopy (ICP-AES), and the results are summarized in Table S1.† The determined atomic ratios fit well with the nominal ones, which also gives evidence for the incorporation of Tb^{3+} into the LDH host matrix. The corresponding TEM image (Fig. 3c) reveals plenty of thin nanoflakes (~2 nm in thickness) intercrossing each other. The HRTEM image (Fig. 3d, inset) shows hexagonally arranged spots for an individual nanoflake of the Tb-ZnCr–LDH, confirming the single crystal nature.[38] A lattice spacing of 0.26 nm is observed, corresponding to the (012) plane of the Tb-ZnCr–LDH phase. This value is in accordance with the in-plane structural parameter of the Tb-ZnCr–LDH crystal determined from the XRD characterization ($d_{012} = 0.25$ nm).

The surface area and porosity properties of these prepared Tb-ZnCr–LDH samples were investigated by low temperature N_2 sorption analysis. As shown in Fig. S3,† typical IV isotherms with an H3-type hysteresis loop are observed in all cases, implying the presence of mesopores.[39] The pore size analysis based on the isotherms shows that these samples exhibit a mesopore distribution in the range of 15–18 nm. Since the surface area is an important factor which influences the photocatalytic performance, the specific surface areas of Tb-ZnCr–LDH samples were obtained and are summarized in Table S2.† The surface area of LDH-0%, LDH-0.1%, LDH-0.5%, LDH-1%, and LDH-5% is 166.6 $m^2\ g^{-1}$, 174.8 $m^2\ g^{-1}$, 187.6 $m^2\ g^{-1}$, 158.3 $m^2\ g^{-1}$, and 165.9 $m^2\ g^{-1}$, respectively. The LDH-0.5% possesses the largest surface area among these Tb-ZnCr–LDH samples, which guarantees a sufficient exposure of active sites and the resulting enhanced photocatalytic behavior.

Fig. 4a shows the UV-vis diffuse reflectance spectra of these Tb-ZnCr–LDH samples. Two absorption bands at 410 nm and 570 nm are observed, which can be attributed to the ligand-to-metal charge-transfer (LMCT) from the 2p orbital of oxygen to the 3d orbital of Cr^{3+} (O 2p → Cr $3dt_{2g}$) and from Cr $3dt_{2g}$ to Cr $3de_g$, respectively. The absorption band in the range of 200–300 belongs to LMCT from the 2p orbital of oxygen to the 3d orbital of Zn.[32] The introduction of Tb^{3+} into the ZnCr–LDH matrix leads to an enhancement of light absorption in the visible-light region. Moreover, the band gap is calculated from the UV-vis diffuse reflectance spectra (Fig. 4a, inset). The band gap of the pristine ZnCr–LDH is ~2.30 eV, which is consistent with the previous reports.[40] After doping with Tb^{3+}, the band gap decreases to 2.26 eV, 2.09 eV, 2.21 eV and 1.70 eV for LDH-0.1%, LDH-0.5%, LDH-1% and LDH-5%, respectively. This further indicates that the light absorption can be effectively extended by narrowing the band gap of the ZnCr–LDH *via* Tb-doping. Photoluminescence (PL) behavior reflects the separation-recombination process of photo-induced charge carriers, where a strong separation ability of photo-induced electron–hole pairs gives rise to a weak photoluminescence signal.[39] In Fig. 4b, the PL emission spectra of the synthesized Tb-ZnCr–LDH are examined at an excitation wavelength of 350 nm, and the intensity decreases as the following sequence: LDH-5% > LDH-0% > LDH-0.1% > LDH-1% > LDH-0.5%. The results reveal that the sample of LDH-0.5% possesses the strongest photo-induced electron–hole separation efficiency resulting from a suitable

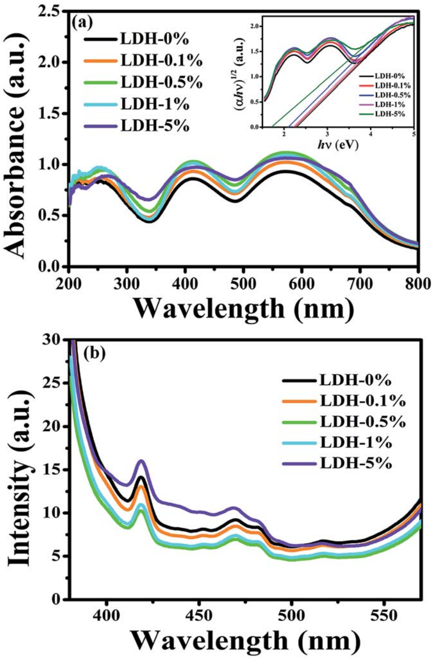

Fig. 4 (a) UV-vis diffuse reflectance and (b) photoluminescence spectra of the Tb-ZnCr–LDH samples with different amounts of Tb. The inset in (a) shows their corresponding plots for the determination of the band gap.

incorporation of Tb^{3+}. However, LDH-5% shows the strongest PL signal, which could be ascribed to the formation of a recombination center of photo-induced electrons and holes caused by an excess amount of Tb^{3+} in the ZnCr–LDH.

Photocatalytic performance of splitting water into O_2 by using the Tb-ZnCr–LDH was studied under visible-light irradiation with $AgNO_3$ as an electron acceptor. The stoichiometric reaction occurs as follows:

$$4Ag^+ + 2H_2O \rightarrow 4Ag + O_2 + 4H^+ \tag{1}$$

Fig. 5a shows the O_2 production from water catalyzed by the Tb-ZnCr–LDH under visible light illumination using a UV cutoff filter ($\lambda > 420$ nm). It is found that the oxygen productivity increases significantly from 543 μmol h^{-1} g^{-1} to 1022 μmol h^{-1} g^{-1} upon the increase of Tb^{3+} doping from 0% to 0.5%, but decreases with a further increase of the Tb^{3+} content. The photocatalytic activity of these Tb-ZnCr–LDH samples displays a sequence: LDH-0.5% (1022 μmol h^{-1} g^{-1}) > LDH-1% (802 μmol h^{-1} g^{-1}) > LDH-0.1% (711 μmol h^{-1} g^{-1}) > LDH-5% (632 μmol h^{-1} g^{-1}) > LDH-0% (543 μmol h^{-1} g^{-1}). The optimum activity is present in the sample of LDH-0.5%, indicating that a suitable Tb^{3+} substitution (*e.g.* 0.5% molar ratio) can largely enhance the photocatalytic performance of the ZnCr–LDH. This will be further discussed in the following section.

The Tb-ZnCr–LDH maintains a nearly constant photocatalytic oxygen production activity over three cycles (Fig. 5b), indicating a satisfactory stability. It is reported that the deposition of sacrificial Ag NPs usually decreases the activity of the photocatalysts during cycling tests.[41] To give a further illustration, HRTEM images of the used Tb-ZnCr–LDH catalyst are shown in Fig. S4,† from which we infer that its plate-like morphology is maintained after three cycling tests (Fig. S4a†). However, just a few silver particles with a diameter of ~10 nm are observed on the surface of LDH nanoplatelets (Fig. S4b†), which is consistent with the EDX elemental analysis results (Fig. S4c,† Ag percentage: 0.18%). Therefore, the stability of the Tb-ZnCr–LDH can be ascribed to the chemical stability of LDH materials. The small amount of Ag deposition does not induce obvious activity loss. The apparent quantum yield (AQY) of LDH-0.5% reaches 55% at 450 nm (Fig. 6a), which is much higher than that of the pure ZnCr–LDH (42% at 450 nm). Moreover, the activity of the Tb-ZnCr–LDH was further investigated through the turnover number (TON) (see the ESI for calculation details†). The sample of LDH-0.5% shows a nearly 2 times larger TON value than pristine ZnCr–LDH (Fig. S5†), further indicating its superior photocatalytic properties.

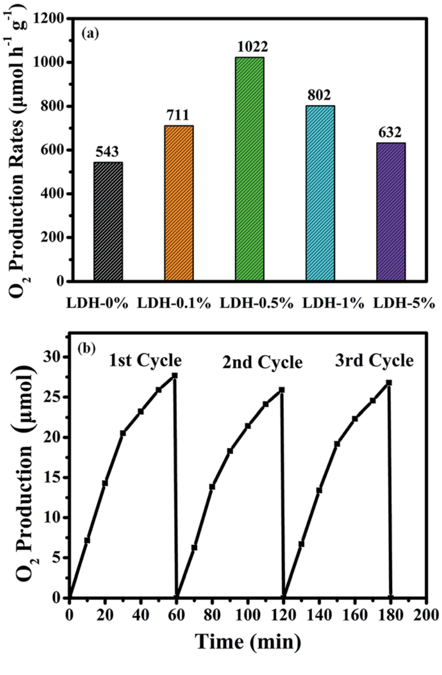

Fig. 5 (a) Oxygen evolution over various Tb-ZnCr–LDH samples in the aqueous suspension under visible light ($\lambda > 420$ nm) irradiation using 1 × 10^{-2} M $AgNO_3$ as a sacrificial agent; (b) catalyst cycling tests for the photocatalytic generation of oxygen from water in the presence of LDH-0.5%.

To investigate the influence of Tb^{3+} doping on the ZnCr–LDH brucite layer, electrochemical impedance spectroscopy (EIS) and photoelectrochemical (PEC) measurements were carried out. The semicircle diameter of EIS equals the electron transfer resistance, which reflects the charge transfer properties of the catalysts. In Fig. S6a,† the Tb^{3+} doped samples show a smaller semicircle diameter compared with the pristine ZnCr–LDH, indicating facile charge transfer by the incorporation of Tb^{3+} into the ZnCr–LDH.[42] However, the sample of LDH-5% gives a relatively poor photocatalytic performance, which is related to its high recombination rate of charge carriers proved by the results of photoluminescence (Fig. 4b). Fig. S6b† displays the linear sweep voltammetry (LSV) curves of Tb-ZnCr–LDH samples upon chopped light illumination. LDH-0.5% gives approximately 1.4 times higher photocurrent density than the

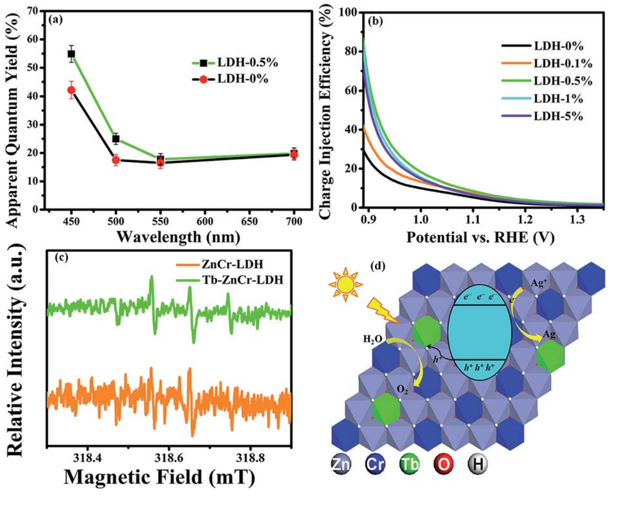

Fig. 6 (a) The apparent quantum yield for the ZnCr–LDH and Tb-ZnCr–LDH, respectively; (b) correlation curves of charge injection efficiency *vs.* potential for various Tb-ZnCr–LDH samples; (c) DMPO spin-trapping ESR spectra recorded for DMPO–$^{\bullet}$OH over LDH-0.5% and pristine ZnCr–LDH, respectively. Conditions: [DMPO] = 0.10 M, m_{cat} = 2 mg, $V_{solvent}$ = 0.5 mL, Xe lamp ($\lambda > 420$ nm), and ambient temperature; (d) schematic illustration of the oxygen evolution process over the Tb-ZnCr–LDH under visible-light irradiation.

pure ZnCr–LDH, further demonstrating the largely improved photocatalytic activity of the ZnCr–LDH by Tb^{3+} doping. The *I–t* curves (Fig. S6c†) illustrate a fast photo-response for the obtained Tb-ZnCr–LDH samples due to the enhanced charge mobility.

The charge injection yield is an important parameter to evaluate the photocatalytic ability, which is also determined to study the charge transfer behavior at the surface of the Tb-ZnCr–LDH. The charge injection yield is obtained according to the following equation:

$$J_{\mathrm{H_2O}} = J_{\mathrm{absorbed}} \times P_{\mathrm{charge\ separation}} \times P_{\mathrm{charge\ injection}} \qquad (2)$$

The photocurrent density of water splitting ($J_{\mathrm{H_2O}}$) is a product of the rate of photon absorption expressed as a current density (J_{absorbed}), the charge separation yield of the photo-induced carriers ($P_{\mathrm{charge\ separation}}$), and charge injection yield to the electrolyte ($P_{\mathrm{charge\ injection}}$).[25,43] Assuming the charge injection yield is 100% ($P_{\mathrm{charge\ injection}} = 1$), the photocurrent is only a product of J_{absorbed} and $P_{\mathrm{charge\ separation}}$ when measured in the electrolyte with H_2O_2 ($J_{\mathrm{H_2O_2}}$):

$$P_{\mathrm{charge\ injection}} = J_{\mathrm{H_2O}}/J_{\mathrm{H_2O_2}} \qquad (3)$$

Therefore, we examined the charge injection efficiency of these Tb-ZnCr–LDH samples with various Tb^{3+} doping contents by comparing the photocurrent from water and H_2O_2 oxidation. The LSV curves under dark conditions and light illumination are provided in Fig. S6d.† The weak current signal under dark conditions for the Tb-ZnCr–LDH is ascribed to the electrochemical oxidation of H_2O_2. Current-potential behavior under light illumination ($\lambda > 420$ nm) in Na_2SO_4 with or without H_2O_2 is recorded and is shown in Fig. S6e.† And the photocurrent increases significantly after adding H_2O_2. Fig. 6b shows the charge injection efficiencies calculated from the photocurrent in the electrolyte of Na_2SO_4 and Na_2SO_4 containing H_2O_2, respectively. The results show that Tb^{3+}-doped ZnCr–LDH materials exhibit much higher charge injection efficiency than the pristine ZnCr–LDH, and the optimal value is presented by the LDH-0.5% sample. A further enhanced amount of Tb^{3+} (>0.5%) leads to a decrease in the charge injection efficiency.

The spin-trapping electron spin resonance (ESR) technique was employed to investigate the presence of a hydroxyl radical ($^{\bullet}OH$) to figure out the redox ability of LDH-0.5% and pristine ZnCr–LDH. The surface OH group captures photo-induced holes to form a hydroxyl radical ($^{\bullet}OH$), which is an essential process in the reaction.[44] According to the previous report,[45] the oxygen evolution reaction scheme is described as follows:

$$H_2O + * \rightarrow *OH + H^+ + e^- \qquad (4)$$

$$*OH \rightarrow *O + H^+ + e^- \qquad (5)$$

$$*O + H_2O \rightarrow *OOH + H^+ + e^- \qquad (6)$$

$$*OOH \rightarrow * + O_2 + H^+ + e^- \qquad (7)$$

The symbol '*' represents the surface of the catalyst. Firstly, a H_2O molecule adsorbs onto the surface of the LDH catalyst followed by deprotonation to produce a hydroxyl radical. The hydroxyl radical undergoes a subsequent oxidation reaction to form *O, which then reacts with another H_2O molecule to produce *OOH. Finally, O_2 is released from *OOH. Fig. 6c shows the ESR spectra of these two samples, with dimethyl pyridine *N*-oxide (DMPO) used as a spin-trapping reagent. The peaks of DMPO–$^{\bullet}OH$ with an intensity ratio of 1 : 2 : 2 : 1 are clearly observed in LDH-0.5%, which is stronger than the undoped ZnCr–LDH. The result verifies that the introduction of Tb induces a more active component ($^{\bullet}OH$), which is the critical intermediate in the water oxidation reaction. This can be ascribed to the improvement in the transport properties of charge carriers through Tb^{3+} doping, as demonstrated by the charge injection measurements.

The proposed scheme for the photocatalytic process of the Tb-ZnCr–LDH is shown in Fig. 6d. The photoluminescence (PL) spectrum shows that a suitable incorporation of Tb^{3+} results in enhanced separation efficiency of photo-induced electron–hole pairs. Moreover, Tb^{3+}-doped ZnCr–LDH materials exhibit much higher charge injection efficiency than the pristine ZnCr–LDH, which reveals that Tb in the LDH matrix acts as a hole acceptor to facilitate the charge injection and surface oxidation process. Consequently, the improved transport properties of charge carriers give rise to an increased $^{\bullet}OH$ generation on the surface of the Tb-ZnCr–LDH (ESR, Fig. 6c), accounting for the largely enhanced photocatalytic activity in the oxygen evolution reaction.

Conclusions

In summary, Tb^{3+}-doped ZnCr–LDH photocatalysts have been prepared by a facile co-precipitation method for solar water splitting. The ZnCr–LDH with suitable Tb^{3+} doping (0.5%) exhibits significantly enhanced photocatalytic efficiency in the visible light range, which is about a 2-fold increase compared with that of the pristine ZnCr–LDH. The large photocatalytic improvement is achieved owing to the efficient separation ability and transfer properties of photo-induced charge carriers by the incorporation of Tb^{3+} into LDH brucite layers. In addition, the favorable transfer environment for charge carriers leads to an efficient charge injection process in the photocatalytic reaction. This material can be used as a promising candidate in the field of high-performance solar energy conversion.

Acknowledgements

This work was supported by the National Natural Science Foundation of China (NSFC), the 973 Program (Grant No. 2014CB932102), the Fundamental Research Funds for the Central Universities (buctrc201506; YS 1406), and the Specialized Research Fund for the Doctoral Program of Higher Education (20130010110013).

Notes and references

1 X. Chen, S. Shen, L. Guo and S. S. Mao, *Chem. Rev.*, 2010, **110**, 6503.
2 Z. Zou, J. Ye, K. Sayama and H. Arakawa, *Nature*, 2001, **414**, 625.
3 K. Maeda, T. Takata, M. Hara, N. Saito, Y. Inoue, H. Kobayashi and K. Domen, *J. Am. Chem. Soc.*, 2005, **127**, 8286.
4 D. Jing and L. Guo, *J. Phys. Chem. B*, 2006, **110**, 11139.
5 A. Kudo and Y. Miseki, *Chem. Soc. Rev.*, 2009, **38**, 253.
6 J. Pfrommer, M. Lublow, A. Azarpira, C. Göbel, M. Lücke, A. Steigert, M. Pogrzeba, P. W. Menezes, A. Fischer, T. Schedel-Niedrig and M. Driess, *Angew. Chem., Int. Ed.*, 2014, **53**, 5183.
7 K. R. Reyes-Gil, E. A. Reyes-Garcia and D. Raftery, *J. Phys. Chem. C*, 2007, **111**, 14579.
8 X. Wang, G. Liu, Z. G. Chen, F. Li, L. Wang, G. Q. Lu and H. M. Cheng, *Chem. Commun.*, 2009, **45**, 3452.
9 G. Zhang, B. Lin, W. Yang, S. Jiang, Q. Yao, Y. Chen and B. Gao, *RSC Adv.*, 2015, **5**, 5823.
10 J. Wang and F. E. Osterloh, *J. Mater. Chem. A*, 2014, **2**, 9405.
11 Y. Wang, Y. Wang, R. Jiang and R. Xu, *Ind. Eng. Chem. Res.*, 2012, **51**, 9945.
12 Q. Wang and D. O'Hare, *Chem. Rev.*, 2012, **112**, 4124.
13 M. Shao, J. Han, M. Wei, D. G. Evans and X. Duan, *Chem. Eng. J.*, 2011, **168**, 519.
14 P. R. Chowdhury and K. G. Bhattacharyya, *Dalton Trans.*, 2015, **44**, 6809.
15 Y. Zhao, B. Li, Q. Wang, W. Gao, C. J. Wang, M. Wei, D. G. Evans, X. Duan and D. O'Hare, *Chem. Sci.*, 2014, **5**, 951.
16 C. G. Silva, Y. Bouizi, V. Fornes and H. Garcıa, *J. Am. Chem. Soc.*, 2009, **131**, 13833.
17 N. Baliarsingh, K. M. Parida and G. C. Pradhan, *Ind. Eng. Chem. Res.*, 2014, **53**, 3834.
18 L. Mohapatra and K. M. Parida, *Phys. Chem. Chem. Phys.*, 2014, **16**, 16985.
19 B. Li, Y. Zhao, S. Zhang, W. Gao and M. Wei, *ACS Appl. Mater. Interfaces*, 2013, **5**, 10233.
20 J. C. G. Bunzli, *Acc. Chem. Res.*, 2006, **2006**, 53.
21 A. W. Xu, Y. Gao and H. Q. Liu, *J. Catal.*, 2002, **207**, 151.
22 J. M. Fernández, C. Barriga, M. A. Ulibarri, F. M. Labajos and V. Rives, *Chem. Mater.*, 1997, **9**, 312.
23 T. Stumpf, H. Curtius, C. Walther, K. Dardenne, K. Ufer and T. Fanghanel, *Environ. Sci. Technol.*, 2007, **41**, 3186.
24 P. Gunawan and R. Xu, *J. Phys. Chem. C*, 2009, **113**, 17206.
25 H. Dotan, K. Sivula, M. Grätzel, A. Rothschild and S. C. Warren, *Energy Environ. Sci.*, 2011, **4**, 958.
26 F. Leroux and C. Taviot-Gueho, *J. Mater. Chem.*, 2005, **15**, 3628.
27 Š. Paušová, J. Krýsa, J. Jirkovský, C. Forano, G. Mailhot and V. Prevot, *Appl. Catal., B*, 2015, **170–171**, 25.
28 D. G. Evans and X. Duan, *Chem. Commun.*, 2006, **42**, 485.
29 M. Domínguez, M. E. Perez-Bernal, R. J. Ruano-Casero, C. Barriga, V. Rives, R. A. S. Ferreira, L. D. Carlos and J. Rocha, *Chem. Mater.*, 2011, **23**, 1993.
30 J. Liang, R. Ma and T. Sasaki, *Dalton Trans.*, 2014, **43**, 10355.
31 T. Posati, F. Costantino, L. Latterini, M. Nocchetti, M. Paolantoni and L. Tarpani, *Inorg. Chem.*, 2012, **51**, 13229.
32 N. Baliarsingh, L. Mohapatra and K. Parida, *J. Mater. Chem. A*, 2013, **1**, 4236.
33 M. d. Arco, V. Rives, R. Trujillano and P. Malet, *J. Mater. Chem.*, 1996, **6**, 1419.
34 Y. Zhao, J. G. Li, F. Fang, N. Chu, H. Ma and X. Yang, *Dalton Trans.*, 2012, **41**, 12175.
35 T. I. T. Okpalugo, P. Papakonstantinou, H. Murphy, J. McLaughlin and N. M. D. Brown, *Carbon*, 2005, **43**, 153.
36 M. J. Guittet, J. P. Crocombette and M. Gautier-Soyer, *Phys. Rev. B: Condens. Matter Mater. Phys.*, 2001, **63**, 125117.
37 Y. Lee, J. H. Choi, H. J. Jeon, K. M. Choi, J. W. Lee and J. K. Kang, *Energy Environ. Sci.*, 2011, **4**, 914.
38 F. Zhang, X. Zhao, C. Feng, B. Li, T. Chen, W. Lu, X. Lei and S. Xu, *ACS Catal.*, 2011, **1**, 232.
39 J. L. Gunjakar, I. Y. Kim, J. M. Lee, N. S. Lee and S. J. Hwang, *Energy Environ. Sci.*, 2013, **6**, 1008.
40 K. Parida, L. Mohapatra and N. Baliarsingh, *J. Phys. Chem. C*, 2012, **116**, 22417.
41 D. K. Zhong, S. Choi and D. R. Gamelin, *J. Am. Chem. Soc.*, 2011, **133**, 18370.
42 G. Zhang, B. Lin, Y. Qiu, L. He, Y. Chen and B. Gao, *Int. J. Hydrogen Energy*, 2015, **40**, 4758.
43 D. K. Zhong, S. Choi and D. R. Gamelin, *J. Am. Chem. Soc.*, 2011, **133**, 18370.
44 T. L. Thompson and J. T. Yates, *Chem. Rev.*, 2006, **106**, 4428.
45 S. M. Xu, T. Pan, Y. B. Dou, H. Yan, S. T. Zhang, F. Y. Ning, W. Y. Shi and M. Wei, *J. Phys. Chem. C*, 2015, **119**, 18823.